

See discussions, stats, and author profiles for this publication at: <https://www.researchgate.net/publication/263953751>

Thin-Film Composite Membranes and Formation Mechanism of Thin-Film Layers on Hydrophilic Cellulose Acetate Propionate Substrates for Forward Osmosis Processes

ARTICLE *in* INDUSTRIAL & ENGINEERING CHEMISTRY RESEARCH · MARCH 2012

Impact Factor: 2.59 · DOI: 10.1021/ie2027052

CITATIONS

63

READS

37

4 AUTHORS, INCLUDING:



Tai-Shung Chung

National University of Singapore

727 PUBLICATIONS 19,581 CITATIONS

SEE PROFILE

Thin-Film Composite Membranes and Formation Mechanism of Thin-Film Layers on Hydrophilic Cellulose Acetate Propionate Substrates for Forward Osmosis Processes

Xue Li,[†] Kai Yu Wang,[‡] Bradley Helmer,[§] and Tai-Shung Chung^{*,†,‡}

[†]NUS Graduate School for Integrative Science and Engineering, and [‡]Department of Chemical & Biomolecular Engineering, National University of Singapore, Singapore 117456, Singapore

[§]Eastman Chemical Company, Kingsport, Tennessee 37663, United States

ABSTRACT: For the first time, the potential of using hydrophilic cellulose acetate propionate (CAP) as microporous substrates for the fabrication of thin-film composite (TFC) forward osmosis (FO) membranes has been explored. Two types of TFC flat sheet membranes with well-designed substrate structures were prepared. The CAP-TFC membranes show very low J_s/J_w ratios (i.e., the ratio of reverse draw solute flux to water flux) of about 0.05 g/L with reasonably high water fluxes under the pressure-retarded osmosis (PRO) mode using 2 M NaCl as the draw solution and deionized water as the feed. When using model seawater as the feed, the water flux is about 12.3 LMH which is comparable to the best in the literature. These results, combined with positron annihilation spectroscopy (PAS) data, confirm the hypothesis that a finger-like morphology in the substrate is not crucial to the performance of TFC FO membranes. Moreover, the surface and skin morphology of the substrate may play essential roles in the formation of the polyamide layer as well as its perfectness and FO performance. A dynamic scheme to elucidate the evolution of forming the globular and worm-like structure during the interfacial polymerization has been proposed. Substrates with larger pores and broader distribution may facilitate rapid migration of amine molecules, induce more complicated convection at the interface, and enlarge reaction contact area, resulting in a rougher but more compact polyamide layer in the TFC membranes, while smaller surface pores of substrate favor simple convection at the interface during the interfacial reaction, producing nascent cross-linked films with smaller domain sizes, smoother and less dense structure, and less defects.

1. INTRODUCTION

Since the global demands for clean water and renewable energy are continuously increasing, water reuse and seawater desalination based on forward osmosis processes and blue energy derived from pressure retarded osmosis (PRO) processes have received worldwide attention. The heart of these emerging technologies is the forward osmosis (FO) membrane. Forward osmosis membranes have been employed in applications for wastewater treatment,¹ desalination,^{2–5} power generation,^{6,7} pharmaceutical concentration,⁸ and food processing.⁹ These processes all rely on the osmotic pressure gradient across the semipermeable membrane between the draw solution and the feed solution. The ideal FO membranes have the characteristics of semipermeable and hydrophilic nature that facilitate water permeation while rejecting other components. Most FO membranes are designed to be asymmetric in configuration and comprise a thin dense layer on top of a porous support, either fabricated by the phase inversion approach^{10–13} or by the interfacial polymerization approach.^{14–19} One typical example is cellulose acetate (CA) FO membranes reported by Zhang et al.²⁰ and Su et al.¹² The CA FO membranes were fabricated via a phase inversion method from which the selective layers were formed simultaneously with the bulk membranes. On the other hand, interfacial polymerization, a predominant method for the fabrication of thin-film composite (TFC) reverse osmosis (RO) membranes,^{21–26} is now being explored for the development of FO membranes due to its previous success on RO membranes and availability of various moieties for the

interfacial polymerization. Since RO and FO are operated under extremely different operation conditions, several problems have been encountered during the development of FO membranes via interfacial polymerization technology.

Traditionally, the TFC RO membranes are constructed on thick porous substrates to mechanically withstand extremely high hydraulic pressures during the desalination process. Application of this protocol for the fabrication of FO membranes will lead to severe internal concentration polarization (ICP) and water flux reduction due to the thick substrates. Unlike the external concentration polarization which can be eliminated by cross or turbulent flow, the effect of ICP in FO processes is an inherent problem for asymmetric FO membranes. Effective ways to mitigate the ICP effect are to (1) reduce substrates' thicknesses,^{13,20} (2) fabricate the substrate with desirable porous morphology,^{20,27} and (3) alter the sublayer's physicochemical properties from hydrophobicity to hydrophilicity.^{19,28} Wang et al.¹⁹ and Widjojo et al.²⁸ have demonstrated that hydrophilic substrates made of blends from polysulfone (PSf) and sulfonated polysulfone improve fluxes. This is because a relatively hydrophobic PSf substrate makes it difficult to be fully wetted in water, thus aggravating the ICP effect and decreasing water flux.

Special Issue: APCCHE 2012

Received: November 22, 2011

Revised: February 15, 2012

Accepted: February 24, 2012

Published: February 24, 2012

Table 1. Physicochemical Properties of CAP Polymers and Membranes

| polymer ID | DS (OH) ^a | DS (Pr) | DS (Ac) | DS (Pr)/(DS(Pr) + DS (Ac)) | contact angle ^b (deg) | contact angle ^c (deg) |
|------------|----------------------|---------|---------|----------------------------|----------------------------------|----------------------------------|
| CAP-I | 0.38 | 0.72 | 1.90 | 0.27 | 72.6 ± 2.7 | 71.7 ± 2.1 |
| CAP-II | 0.82 | 0.54 | 1.64 | 0.25 | 68.2 ± 3.4 | 68.1 ± 4.0 |

Notes:

^aDS: degree of substitution. ^bDense membranes. ^cTop surface of porous membranes.

Fundamental understanding of desirable sublayer morphology and the effect of its physicochemical properties on FO performance is urgently needed. Not only does sublayer affect the degree of internal concentration polarization but also fouling characteristics and backwashing efficiency.^{29–33} In addition, the formation mechanism of the rough ridge-valley morphology on the interfacial polymerized polyamide layer must be re-examined because the required flawlessness of the thin polyamide layer in FO is much higher than that in RO. In fact, the interfacial polymerized polyamide layer is intrinsically defective if tests are conducted under no or low hydraulic pressures such as FO,^{16–19,28} but it can exhibit an extremely high salt rejection (>99.4%) under extremely high pressures such as RO. This is because a high pressure can induce more ordered conformation,³⁴ resulting in tightened polymer chains and a polyamide layer with few defects.

Various hypotheses have been proposed on desirable substrate morphology for the fabrication of high-performance TFC membranes. Some works suggested that macrovoids are essential for the high FO flux,^{15,16} while Widjojo et al.²⁸ demonstrated otherwise by casting blends from polysulfone (PSf) and sulfonated polysulfone as porous substrates. Mechanisms to form the rough ridge-valley polyamide layer after interfacial polymerization have been proposed.^{35,36} They are useful but insufficient to explain the observed worm-like surface morphology. The performance of FO membranes is strongly determined by two factors: (1) the polyamide layer that controls water flux, salt rejection, and reverse draw solute flux, and (2) the sublayer that not only provides mechanical strength and flow channels, but also determines the degree of ICP and the effective osmotic gradient for water flux. The aims of this work are to investigate the fundamental science of both factors.

For the first time, structurally tailored hydrophilic cellulose acetate propionate (CAP) is used as the porous substrate for the fabrication of TFC FO membranes. CAP was chosen as the substrate material because of its abundant source, reasonably low cost, ease of processability, and most importantly its tunability of hydrophilicity. It was used for RO processes in the 1970s.^{37,38} Here, two types of CAP polymers with different content of OH groups in the repeating unit were synthesized by Eastman Chemicals. The increase in OH group content enhances hydrophilicity. In addition to being the basis of developing high performance FO membranes, these two CAPs give us tools to study the effects of material hydrophilicity on substrate morphology, interfacial polymerization, and membrane performance (i.e., flux, rejection rate, and reverse flux of draw solute). Both sponge-like and finger-like substrates are employed to fabricate CAP-TFC membranes following a two-step procedure: (1) casting the CAP substrate by phase inversion; (2) synthesizing the polyamide dense layer on top of the CAP substrate via the *in situ* interfacial polymerization between two monomer solutions in different phases. The resultant CAP-TFC membranes are characterized by advanced analytic tools and evaluated in FO processes.

In addition, significant attention is given to investigate the formation mechanism of the rough globular and worm-like surface morphology on the polyamide layer after interfacial polymerization. It is believed that this work may have high impact on the development of next generation FO membranes.

2. EXPERIMENTAL SECTION

2.1. Materials and Chemicals. **2.1.1. Materials and Chemicals for Preparing and Characterizing Substrates.** Cellulose acetate propionate (CAP) with two different degrees of substitution (DS) was kindly provided by Eastman Chemical Company. They are CAP 141-20 and CAP 30735 603-121-A (referred to as CAP-I and CAP-II, respectively). Table 1 lists their characteristic properties and Figure 1 shows the chemical

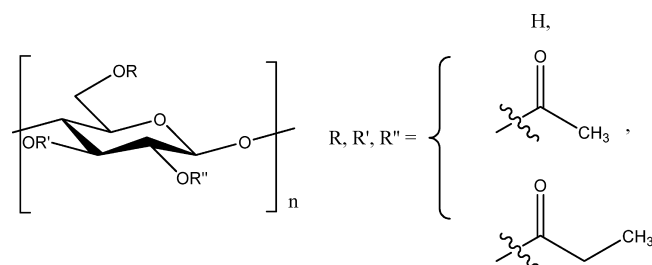


Figure 1. The chemical structure of CAP.

structure. The solvent *N*-methyl-2-pyrrolidinone (NMP, >99.5%) and nonsolvent polyethylene glycol 400 (PEG, M_n = 400 g/mol) were purchased from Merck. The deionized (DI) water used in experiments was produced by a Milli-Q ultrapure water system (Millipore, USA). Polyethylene glycol 35 000 (PEG, M_n = 35 000 g/mol, Merck), polyethylene glycol 40 000 and 60 000 (PEG, M_n = 40 000 g/mol, and M_n = 60 000 g/mol, Nanocs), polyethylene oxide 10 000, 200 000, and 300 000 (PEO, M_n = 100 000 g/mol, M_n = 200 000 g/mol, and M_n = 300 000 g/mol, Sigma-Aldrich) were used to measure the pore size of membrane substrates.

2.1.2. Materials and Chemicals for Preparing the Thin Selective Layer of TFC Membranes. The monomers, *p*-phenylenediamine (PPD, > 99%) and 1,3,5-benzenetricarbonyl trichloride (TMC, 98%) were purchased from Sigma-Aldrich Chemical Co. The solvent heptane (99%) and sodium chloride (NaCl, 99.5%) for membrane performance tests were purchased from Merck. All chemicals were used as received.

2.2. CAP Substrates Fabrication. The CAP substrates were prepared by the Loeb-Sourirajan wet-phase inversion method. Before use, the CAP polymers were dried overnight at 70 ± 5 °C in a vacuum oven (2 mbar) to remove moisture content. Preparation conditions for all substrates are listed in Table 2. The dope solutions were cast on flat glass plates, followed by immersing them into tap water to form porous substrates. After being peeled off from the glass plate, the resultant membranes were rinsed with tap water for 6 h to remove the residual

Table 2. Preparation Conditions and the Shear Viscosity of CAP Dope Solutions

| dope solution | dope solution (wt%) | | | | shear viscosity at shear rate of 10 s ⁻¹ (Pa · s) |
|---------------|---------------------|------|---------|----------|--|
| | polymer | NMP | PEG 400 | DI water | |
| CAP-I | 10 | 43.5 | 43.5 | 3 | 19.7 |
| CAP-II | 10 | 43.5 | 43.5 | 3 | 10.7 |
| CAP-II' | 10 | 27 | 60 | 3 | 24.6 |

solvent and PEG, followed by annealing in DI water at 50 °C for 12 h.

2.3. CAP-TFC Membrane Fabrication. TFC polyamide membranes were prepared on the top side of CAP substrates by interfacial polymerization.³⁹ The procedure was as follows: (1) sealed the backside of the CAP substrate, (2) placed the CAP substrate in an aqueous solution of 1.1 wt % PPD for 1.5 min, and (3) ensured only the top side of the substrate in contact with the solution. After that the excess PPD solution was poured off and the residual drops on the substrates were removed by a rubber roller. Then the substrate was soaked in a solution of 0.2 wt % TMC in heptane for a 20-s polymerization reaction followed by a 10-min air-dry. Finally, the resulting membrane was washed thoroughly with methanol and DI water.

2.4. Characterizations. **2.4.1. Mean Effective Pore Size, Pore Size Distribution, and Porosity of CAP Substrates.** Pore sizes of membrane substrates were measured through the solute transport method. Similar methods have been reported elsewhere.^{40,41} PEG/PEO solutions (200 ppm) with different molecular weights were used to measure the solute rejection under a hydraulic pressure difference of 3 bar. The concentrations of the neutral solutes were measured by a total organic carbon analyzer (TOC ASI-5000A, Shimadzu, Japan).

The measured feed (C_f) and permeate (C_p) concentrations were used for the calculation of the effective solute rejection coefficient R_s (%)

$$R_s (\%) = \left(1 - \frac{C_p}{C_f}\right) 100 \quad (1)$$

Generally, a relationship between solute radius r_s and its molecular weight M_w can be written as follows:⁴²

$$\log_{10} r_s = -1.3363 + 0.395 \log_{10} M_w \quad (2)$$

Therefore, the solute diameters d_s (nm) of PEG (eq 3) and PEO (eq 4) can be determined:^{20,40}

$$d_s = 3.35 \times 10^{-2} M_w^{0.557} \quad (3)$$

$$d_s = 2.09 \times 10^{-2} M_w^{0.587} \quad (4)$$

The mean effective pore size and the pore size distribution were then obtained according to the traditional solute transport approach by ignoring influences of the steric and hydrodynamic interaction between solute and membrane pores, the mean effective pore size (μ_p) and the geometric standard deviation (σ_p) can be assumed to be the same as μ_s (the geometric mean size of solute at $R_s = 50\%$) and σ_s (the geometric standard deviation defined as the ratio of the d_s at $R_s = 84.13\%$ over that at $R_s = 50\%$). As well, the molecular weight cutoff (MWCO) was found at $R_s = 90\%$. Therefore, on the basis of μ_p and σ_p , the

pore size distribution of a membrane can be expressed as the following probability density function:⁴³

$$\frac{dR(d_p)}{dd_p} = \frac{1}{d_p \ln \sigma_p \sqrt{2\pi}} \exp \left[-\frac{(\ln d_p - \ln \mu_p)^2}{2(\ln \sigma_p)^2} \right] \quad (5)$$

Membrane porosity was determined by testing the wet membrane weight, m_1 (g), and the dry membrane weight, m_2 (g). The membrane porosity can be calculated from eq 6:

$$\varepsilon (\%) = \frac{(m_1 - m_2) \div \rho_w}{(m_1 - m_2) \div \rho_w + m_2 \div \rho_p} 100 \quad (6)$$

where ε , ρ_w , and ρ_p indicate the membrane porosity (%), density of water (g/cm³), and density of polymer (g/cm³), respectively.

2.4.2. Characterization of Shear Viscosity of CAP Dope Solutions. The shear viscosity of dope solutions was characterized by an advanced rheological extension system (ARES) Rheometric scientific rheometer (Rheometrics, USA) at low shear rates with a 25 mm cone-and-plate geometry at 25 °C. The steady-state controlled shear rate mode was altered in the range of 1–100 s⁻¹. The power-law model was applied to fit the rheological data and to express the relationship between shear stress τ_s (N m⁻²) and shear rate $\dot{\gamma}$ (s⁻¹) as follows:

$$\tau_s = K \dot{\gamma}^n \quad (7)$$

where K is the power law coefficient constant and n is the power law index.

2.4.3. Contact Angle Measurements. The water contact angle of CAP membranes at 25 °C was measured by a contact angle goniometer (Rame Hart) using Milli-Q DI water as the probe liquid to characterize the hydrophilicity of membranes. During measurements, immediate contact angles were taken and calculated by the software once water drops touch the sample surface. The CAP flat-sheet dense membranes were fabricated using a solution-casting method. NMP was adopted to dissolve the CAP polymers. The nascent membranes were formed after slow evaporation of most solvent and further dried at 80 °C under vacuum for 3–4 days to remove the residual solvent. To minimize the experimental error, 10 readings were measured randomly at different locations and an average contact angle for each condition was calculated.

2.4.4. Determination of Transport Properties of CAP-TFC Membranes in RO Tests. The water permeability, A , salt rejection, R_s , and salt permeability, B , of the CAP-TFC membranes were determined by testing the membranes under the RO mode in both cross-flow and dead-end tests. Cross-flow experiments were conducted in a consecutive lab-scale filtration setup containing a cross-flow permeation cell with an effective membrane area of 17.35 cm² supported by a porous stainless steel spacer, described elsewhere.⁴⁴ Dead-end filtration setup with an effective membrane area of 7.06 cm² was also described clearly in our previous studies.^{12,13,40,41,45} The testing temperature was at 24 ± 1 °C. The water permeability, A , was obtained from the pure water permeation flux under an applied pressure, ΔP , of 1.0 bar. The salt rejection, R_s , was tested under a trans-membrane pressure of 1 bar using 200 ppm NaCl feed solution based on conductivity measurements by a conductivity meter (Schott Instruments GmbH, Germany).

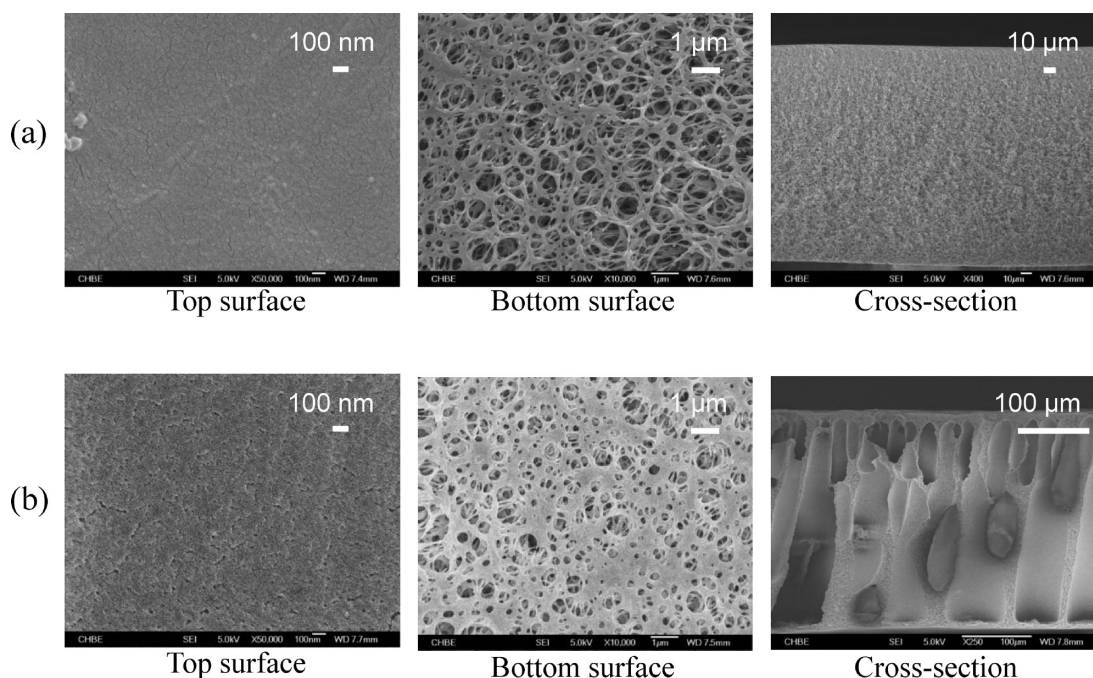


Figure 2. Morphology of the (a) CAP-I substrate, (b) CAP-II substrate.

The salt permeability, B , was derived from the solution-diffusion theory as follows:^{6,46}

$$B = A \frac{(1 - R_s)(\Delta P - \Delta \pi)}{R_s} \quad (8)$$

where $\Delta \pi$ is the osmotic pressure difference across the membrane.

2.4.5. Determination of CAP-TFC Membranes Performance in FO Tests and Evaluation of Structural Parameters of Substrates. FO experiments conducted in this work are similar to those of our previous studies.^{19,20,27,28,45} The experimental system contains a cross-flow filtration cell of 2.0 cm² filtration area. Both the draw solution (NaCl solution with different concentrations) and the feed solution (DI water or 3.5 wt % NaCl solution) counter-currently flowed through the filtration cell at a volumetric flow rates of 0.25 L/min and were recirculated during experiments. Two different membrane orientations were tested at 24 ± 1 °C, with either selective layer against the draw solution (referred to as the pressure retarded osmosis (PRO) mode) or against the feed solution (referred to as the FO mode).

The water permeation flux, J_w (L m⁻² h⁻¹, LMH), is calculated from eq 9 based on the absolute weight change of the feed and the effective membrane area, A_m (m²):

$$J_w = \frac{\Delta \omega}{\Delta t} \frac{1}{A_m} \quad (9)$$

where $\Delta \omega$ (kg) is the absolute weight change of water permeated through the membrane over a predetermined time Δt (h) during the FO tests.

The reverse salt flux, J_s (g m⁻² h⁻¹, gMH) was determined from the conductivity increment in the feed when DI water was used as the feed solution:

$$J_s = \frac{(C_t V_t) - (C_0 V_0)}{\Delta t} \frac{1}{A_m} \quad (10)$$

where C_t (mol L⁻¹) and V_t (L) are the salt concentration and the volume of the feed solution at time t , respectively; C_0 (mol L⁻¹) and V_0 (L) are the initial salt concentration and the volume of the feed solution, respectively.

Theoretically, the relationship between water flux and driving force in a FO process, where external concentration polarization is assumed negligible, under the PRO mode is described as^{5,6}

$$J_w = \frac{1}{K_m} \ln \frac{A \pi_{D,m} - J_w + B}{A \pi_{F,b} + B} \quad (11)$$

In the FO mode, eq 12 is applied:

$$J_w = \frac{1}{K_m} \ln \frac{A \pi_{D,b} + B}{A \pi_{F,m} + J_w + B} \quad (12)$$

where $\pi_{D,m}$ and $\pi_{D,b}$ are the membrane surface osmotic pressure and the bulk osmotic pressure of the draw solution, respectively; $\pi_{F,m}$ and $\pi_{F,b}$ are the membrane surface osmotic pressure and the bulk osmotic pressure of the feed solution, respectively; K_m refers to the solute resistivity from which membrane structural parameter, S_t , can be determined:

$$S_t = K_m D_s \quad (13)$$

where D_s is the salt diffusivity, which has been summarized by researchers.⁴⁷ Structural parameter is related to tortuosity, τ , porous layer thickness, l , and porosity, ϵ , by

$$S_t = \frac{l \tau}{\epsilon} \quad (14)$$

2.4.6. Study of Membrane Morphology and Topology.

The morphology and topology of membranes were examined by field emission scanning electronic microscopy (FESEM, JEOL JSM-6700F) and atomic force microscopy (AFM, Nanoscope IIIa from Digital Instruments). Before FESEM tests, samples were prepared in liquid nitrogen followed by

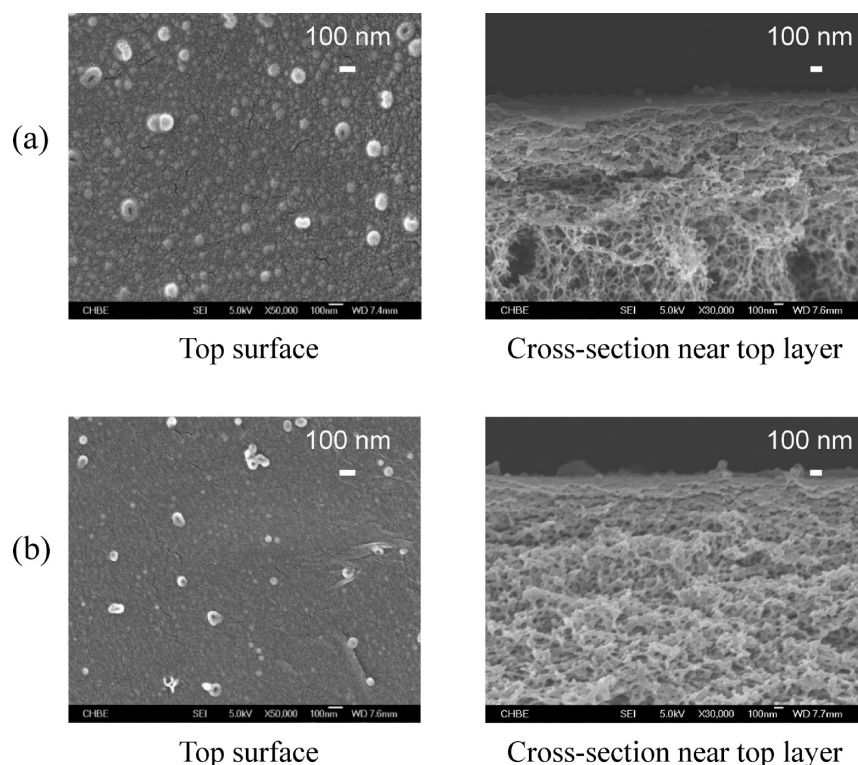


Figure 3. Morphology of the (a) CAP-I-TFC membrane, (b) CAP-II-TFC membrane.

platinum coating using a Jeol JFC-1100E ion sputtering device. AFM tests were using the tapping mode at a scanning rate of 1.2 Hz.

2.4.7. Positron Annihilation Spectroscopy (PAS). Positron annihilation spectroscopy (PAS) was used for membrane characterization.^{48–50} Doppler broadening energy spectra (DBES) using PAS coupled with a slow positron beam was detected for the depth profile of membrane cavity in CAP-TFC membranes. An HP Ge detector at a counting rate of approximately 4800 cps was used to record Doppler broadening energy spectra, and the total number of counts for each spectrum was 1.0 million. *S* parameter and *R* parameter are two important values to express Doppler broadening energy spectra. The former is defined as the ratio of integrated counts between 510.3 and 511.7 keV, while the latter refers to the ratio of the total counts from the valley region with an energy width between 364.2 and 496.2 keV (from 3γ annihilation) to those from the 511 keV peak region with a width between 504.35 and 517.65 (from 2γ annihilation).^{51,52} In other words, *S* parameter is correlated to the changes of the positron and positronium states resulting from free volume changes, while *R* parameter gives information of larger holes in the nanometer to micrometer range. After being fitted by using the VEPFIT program, the PAS result shows the membrane depth profile as a function of incident position energy expressed in terms of depth:

$$Z(E_+) = \frac{40}{\rho} E_+^{1.6} \quad (15)$$

where *Z* is the depth (nm), ρ refers to the density of the polymer (g/cm^3), and E_+ is the incident positron energy (keV).

3. RESULTS AND DISCUSSION

3.1. Characteristic Properties and Morphologies of CAP Membranes. Table 1 shows the degree of substitution in

terms of propionates and acetates in CAP materials as well as the contact angles of CAP dense membranes and the top surface of CAP porous substrates. These two CAP materials share a similar substitution ratio of propionates to the total substitution degree of propionates and acetates. Meanwhile, they have different unsubstituted OH groups. The experimental data confirm the hydrophilic characteristics of these two CAP materials. The contact angle decreases (i.e., more hydrophilic) with an increase in unsubstituted OH groups. Clearly, the hydrophilicity of CAP membranes could be effectively manipulated by controlling the unsubstituted OH groups. This tunability of CAP materials provides a convenient platform for the fabrication of desirable FO membranes.

Figure 2 illustrates the morphologies of CAP substrates. Both CAP-I and CAP-II substrates have similar asymmetric structures with a nanoporous top surface and a fully porous bottom layer. However, their cross-section morphologies are different. The CAP-I substrate has a macrovoid-free sponge-like structure, while the CAP-II substrate possesses a finger-like structure spanning most of the cross-section. The variation of cross-section structure from the sponge-like CAP-I substrate to the finger-like CAP-II substrate is mainly due to the change in dope viscosity (Table 2). The lower dope viscosity promotes the nonsolvent intrusion, and hence produces the macrovoids. Figure 3 shows the morphologies of CAP-TFC membranes after interfacial polymerization. Although the CAP-I-TFC and CAP-II-TFC membranes possess different bulk substrate morphologies, both of them show similar surface structures. The FESEM images confirm the formation of a thin-film dense layer over the porous substrate. It is found that the thin layers are around 200 nm in thickness. However, the thicknesses are not able to be accurately detected by FESEM measurements due to the heterogeneity of rough surfaces. To further

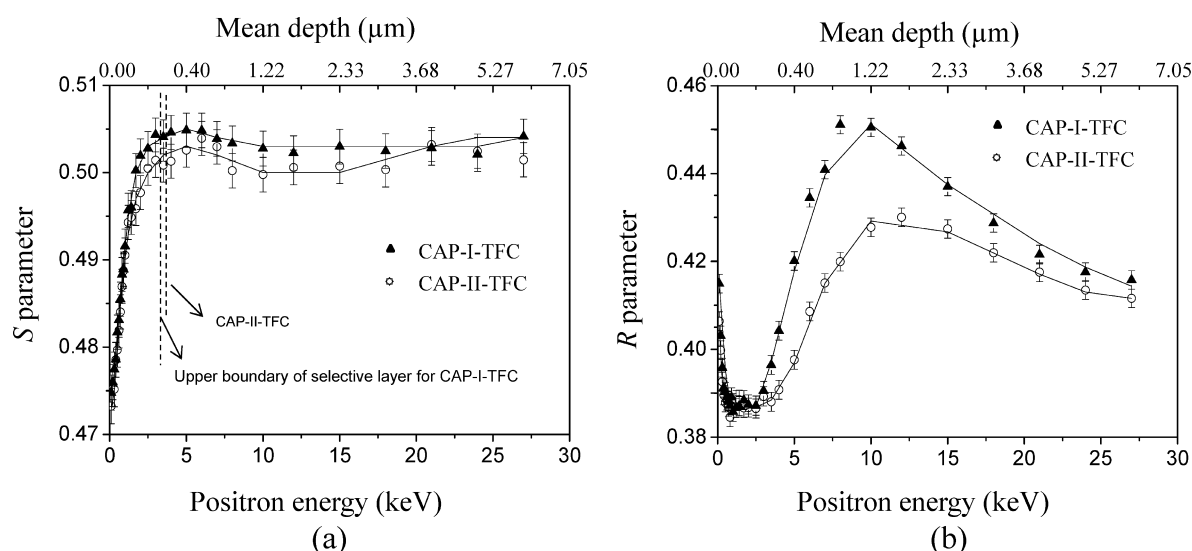


Figure 4. S parameter (a) and R parameter (b) as a function of positron energy for CAP-TFC membranes. The dots are experimental data, and the lines are a fitted curve via VEPFIT fitting.

Table 3. Characteristic Properties of CAP-TFC Membranes

| membrane ID | testing method | water permeability ^a , <i>A</i> (L m ⁻² h ⁻¹ bar ⁻¹) | salt permeability ^a , <i>B</i> (L m ⁻² h ⁻¹) | salt rejection ^a (%) | <i>S_t</i> ^b (m) |
|-------------|----------------|---|--|---------------------------------|---------------------------------------|
| CAP-I-TFC | cross-flow | 1.82 | 0.188 | 89.2 ± 4.5 | 7.89 × 10 ⁻⁴ |
| | dead-end | 1.69 | 0.175 | 88.9 ± 3.7 | 7.64 × 10 ⁻⁴ |
| CAP-II-TFC | cross-flow | 1.42 | 0.132 | 90.5 ± 3.4 | 6.95 × 10 ⁻⁴ |
| | dead-end | 1.36 | 0.126 | 90.4 ± 3.1 | 6.80 × 10 ⁻⁴ |

^aNaCl (200 ppm) as the feed solution in the RO test under an applied pressure of 1 bar. ^bAverage value of 1.5 M and 2.0 NaCl as the draw solution, respectively, and DI water as the feed solution in the FO mode.

investigate the depth profile of TFC membranes, positron annihilation spectroscopy (PAS) tests were conducted.

3.2. Membrane Morphologies Characterized by PAS.

PAS has been effectively used to investigate the depth profile of membranes in our previous studies.^{53,54} Figure 4 shows the S and R parameters versus positron incident energy or the corresponding mean depth of CAP-TFC membranes. The low value of S parameter near the membrane surface is due to the positrons diffusion from surface back into vacuum.^{20,45,48,49} With an increase in positron incident energy, the S parameter increases until the maximum is reached. As stated in the literature,⁵² the variation of the S parameter is an indication of the layer changing ascribed to the variation in both free-volume properties and the chemical structure from the polyamide selective layer to the CAP substrate. The VEPFIT program was used to fit the S parameter curve as a function of the mean depth of CAP-TFC membranes, where a four-layer model was employed for both two membranes. For a thin-film composite membrane, the four-layer model would be employed to better describe the membrane structure: the polyamide dense layer, subsupporting layer incorporated of polyamide (transition layer I), a transition porous layer from subnanopores to micropores (transition layer II), and the bulk porous layer. The simulation curves of four-layer models fit the experimental data closely. The results show that both CAP-TFC membranes are of similar selective layer thicknesses, which agree well with the FESEM images, namely, 177.2 ± 8.7 nm for the CAP-I-TFC membrane and 209.2 ± 49.5 nm for the CAP-II-TFC membrane. The double transition layer for the CAP-I-TFC membrane is with the total thickness of 848.0 ± 119.7 nm, while it is 2575.1 ± 364.6 nm for the CAP-II-TFC

membrane; a bulk porous layer is indicated as the fourth layer without thickness measurement. A comparison of S parameter for the selective layer provides some clues to the compactness of polyamide cross-linking structure as well as to the size of cavities in the polyamide layer as follows: the selective layer of the CAP-I-TFC membrane has a slightly higher S parameter value (i.e., free volume) than that of the CAP-II-TFC membrane (i.e., $0.5050 \pm 4.91 \times 10^{-4}$ vs $0.4996 \pm 6.30 \times 10^{-4}$). The depth profile shown in Figure 4b describes the R parameter as a function of distance from the top membrane surface. With an increase in incident positron energy to about 1 keV, the R parameter value decreases to the minimum, which indicates the dense layer structure of the TFC membrane. Then the R parameter value gradually increases as an ascent while it reaches a progressive transition layer from the dense layer to the porous substrate. This ascent with a higher R parameter value represents the existence of larger cavities in the transition layer and more porous morphology in this region. Therefore, the CAP-I-TFC membrane has a large-pore structure in the transition layer of the substrate in comparison to the CAP-II-TFC membrane, even though the latter possesses many finger-like macrovoids while the former does not.

3.3. Membrane Transport Properties, FO performance and Structural Parameters of CAP-TFC Membranes.

Table 3 summarizes the membrane transport properties such as water permeability coefficient *A* and salt permeability coefficient *B* of CAP-TFC membranes determined in the RO mode. Generally, water permeability and salt permeability are higher for the CAP-I-TFC membrane than those for the CAP-II-TFC membrane in both dead-end and cross-flow tests. *A* values are $1.82 \text{ L m}^{-2} \text{ h}^{-1} \text{ bar}^{-1}$ (cross-flow test) and

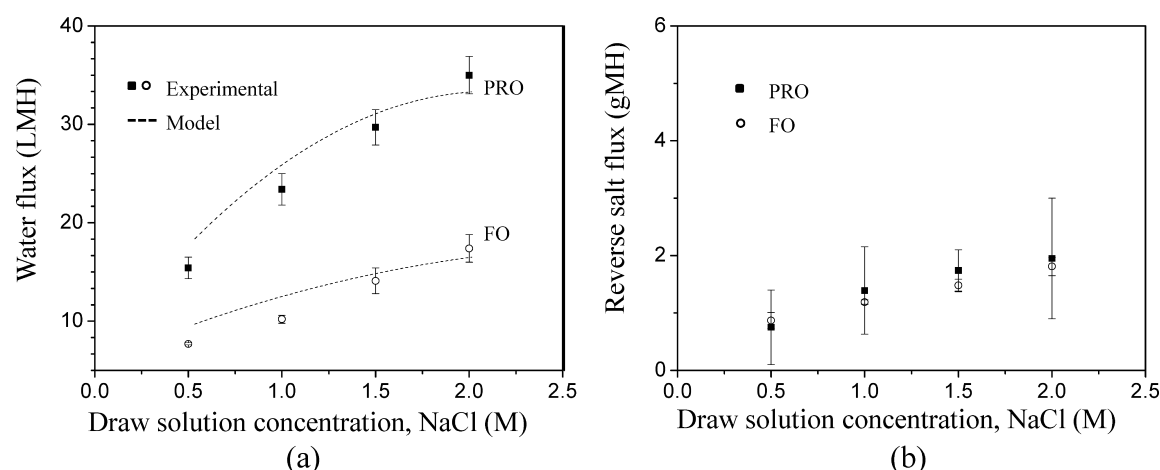


Figure 5. Water flux (a) and reverse salt flux (b) for the CAP-I-TFC membrane under DI water as the feed solution against different draw solution concentration. Structural parameters used for model calculation: cross-flow mode; linear velocity = 5.95 cm/s.

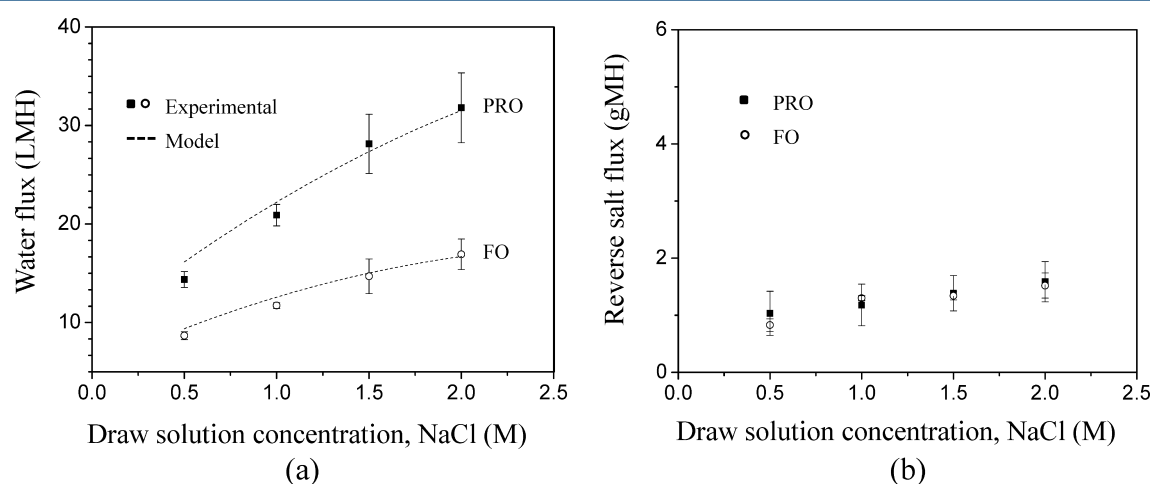


Figure 6. Water flux (a) and reverse salt flux (b) for the CAP-II-TFC membrane under DI water as the feed solution against different draw solution concentration. Structural parameters used for model calculation: cross-flow mode; linear velocity = 5.95 cm/s.

Table 4. Comparison of FO Performance

| membrane | membrane orientation | water flux ($\text{L m}^{-2} \text{h}^{-1}$) | reverse salt flux ($\text{g m}^{-2} \text{h}^{-1}$) | J_s/J_w (g/L) | draw solution (M NaCl) | ref |
|---------------------------|----------------------|--|---|-----------------|------------------------|--------------|
| CAP-I TFC ^a | PRO mode | 35.0 | 1.9 | 0.056 | 2.0 | present work |
| CAP-II TFC ^a | PRO mode | 31.8 | 1.6 | 0.050 | 2.0 | present work |
| PSf TFC ^a | FO mode | 18.2 | — | — | 1.5 | 16 |
| PSf TFC ^a | FO mode | 25.0 | — | — | 1.0 | 18 |
| PES/PESU TFC ^a | PRO mode | 33.0 | 3.7 | 0.112 | 2.0 | 28 |
| PES/SPSf TFC ^a | PRO mode | 24.1 | 4.5 | 0.187 | 0.5 | 19 |
| PSf TFC ^a | PRO mode | 20.5 | 5.9 | 0.288 | 0.5 ^c | 55 |
| PES TFC ^b | PRO mode | 32.2 | 3.5 | 0.109 | 0.5 | 15 |
| PES TFC ^b | PRO mode | 42.6 | 4.0 | 0.094 | 0.5 | 17 |
| HTI-CTA ^a | FO mode | 13.0 | 10.2 | 0.785 | 2.0 | 56 |
| HTI-CA ^a | PRO mode | 18.8 | — | — | 0.5 | 57 |

^aFlat sheet membranes. ^bHollow fiber membranes. ^cFeed solution: 10 mM NaCl.

$1.69 \text{ L m}^{-2} \text{h}^{-1} \text{bar}^{-1}$ (dead-end test) for the CAP-I-TFC membrane and $1.42 \text{ L m}^{-2} \text{h}^{-1} \text{bar}^{-1}$ (cross-flow test) and $1.36 \text{ L m}^{-2} \text{h}^{-1} \text{bar}^{-1}$ (dead-end test) for the CAP-II-TFC membrane. On the other hand, in comparison with those of the CAP-I-TFC membrane, B values for the CAP-II-TFC membrane are lower. These results suggest that although a cross-flow filtration is the preferred method for the RO mode test, a dead-end cell with intense agitation could effectively reduce external concentration polarization as well.

Furthermore, the variations of both A and B values in these two TFC membranes are consistent with the difference in S parameter of their selective layers shown in Figure 4. In other words, the higher pure water permeability and higher salt permeability of the CAP-I-TFC membrane may be attributable to the thinner but less compact polyamide layer. Table 3 also indicates that the CAP-I-TFC and CAP-II-TFC membranes have reasonably high salt rejections against NaCl even at 1 bar.

FO experiments were conducted by using a cross-flow filtration setup. Figures 5 and 6 show the experimental water flux and reverse salt flux of CAP-TFC membranes as a function of draw solution concentration. It can be found that the water flux of the CAP-I-TFC membrane is higher than that of the CAP-II-TFC membrane, while their reverse salt fluxes are of comparable values. Using a 2.0 M NaCl draw solution under the PRO mode, the J_s/J_w ratios (i.e., the ratio of reverse draw solute flux to water flux) of 0.056 g/L and 0.050 g/L were obtained for the CAP-I-TFC membrane and the CAP-II-TFC membrane, respectively. The J_s/J_w ratios of CAP-TFC membranes, a practical indicator of the degree of nonperfectness of a semipermeable membrane in FO processes, are considerably lower in comparison with either commercial FO membranes or other FO membranes reported in literature, as shown in Table 4.^{15–19,28,55–57} Figures 5 and 6 also show comparisons between the experimental water flux and the model prediction curves. The experimental data are substantially consistent with the predictions for CAP-TFC membranes. The model curves fit experimental flux well in both Figures 5 and 6. When using the model 3.5 wt % NaCl solution as the feed solution, the water flux of CAP-TFC membranes as a function of draw solution concentration under the PRO mode is tabulated in Table 5. Almost identical water fluxes of 12 LMH are obtained,

Table 5. Water Fluxes of CAP-TFC Membranes under the Model 3.5 wt % NaCl Solution as the Feed Solution^a

| membrane ID | water flux against 1.0 M NaCl draw solution (L m ⁻² h ⁻¹) | water flux against 1.5 M NaCl draw solution (L m ⁻² h ⁻¹) | water flux against 2.0 M NaCl draw solution (L m ⁻² h ⁻¹) |
|-------------|--|--|--|
| CAP-I-TFC | 6.3 | 9.8 | 11.7 |
| CAP-II-TFC | 6.7 | 9.1 | 12.3 |

^aPRO mode was employed.

indicating that both CAP-I-TFC and CAP-II-TFC membranes may be applicable for seawater desalination.

The reverse salt flux and salt rejection of the TFC membranes are mainly dependent on the selective layer. On the other hand, the water flux and pure water permeability are determined by the selective layer together with the porous substrate. Although the CAP-II-TFC membrane has a straight finger-like morphology which may reduce the diffusion resistance and mitigate the ICP effect, the water flux and pure water permeability are lower than that of the CAP-I-TFC. This might be due to the effect of small-pore structure existing immediately beneath the TFC layer. As displayed in Figure 4b, a lower *R* parameter can be seen clearly in the transition layer of the CAP-II-TFC membrane, indicating smaller cavities beneath the TFC layer on top of the CAP-II substrate in comparison with that of the CAP-I substrate. These small cavities lead to increase the diffusion resistance and result in a lower water flux. In addition, a lower *S* parameter value of the selective layer in the CAP-II-TFC membrane also implies a more compact polyamide layer inducing a lower pure water permeability than that of the CAP-I-TFC membrane.

3.4. Effects of Pore Morphology in the Substrates on the Formation of the Polyamide Layer. From the above discussion, it is clear that the top surface and skin morphology of the substrate other than the bulk morphology plays a crucial role in the formation of polyamide layer as well as the FO performance of the resultant TFC membranes. To better

Table 6. Characteristic Properties of CAP Substrates

| membrane ID | porosity (%) | mean pore diameter (nm) | MWCO (kDa) | geometric standard deviation |
|-------------|--------------|-------------------------|------------|------------------------------|
| CAP-I | 85.8 | 15.3 | 136.0 | 1.31 |
| CAP-II | 85.2 | 18.8 | 218.0 | 1.38 |
| CAP-II' | 84.9 | 22.7 | 327.7 | 1.45 |

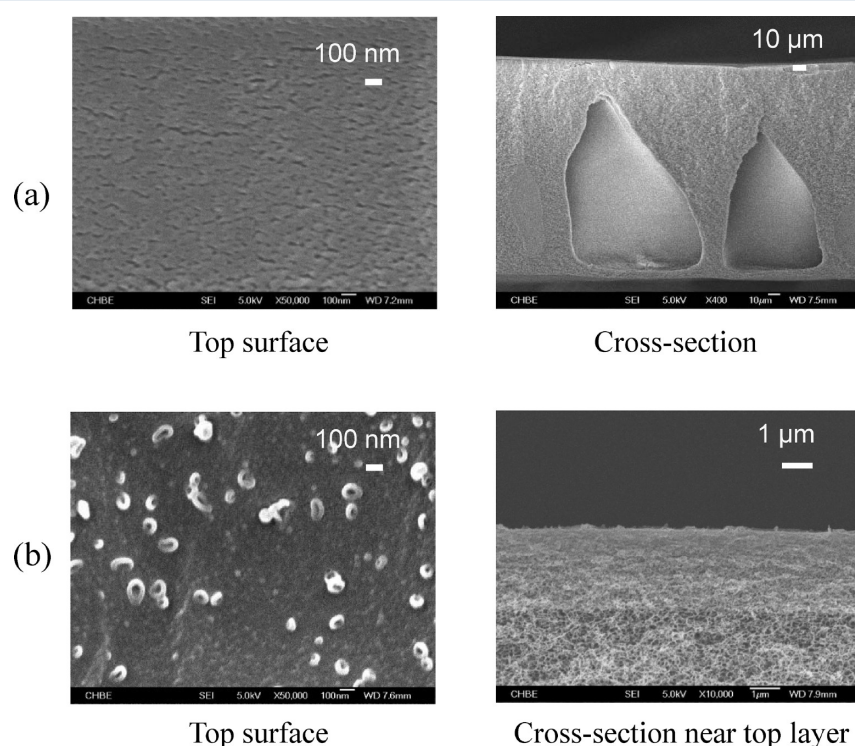


Figure 7. Morphology of the (a) CAP-II' substrate, (b) CAP-II'-TFC membrane.

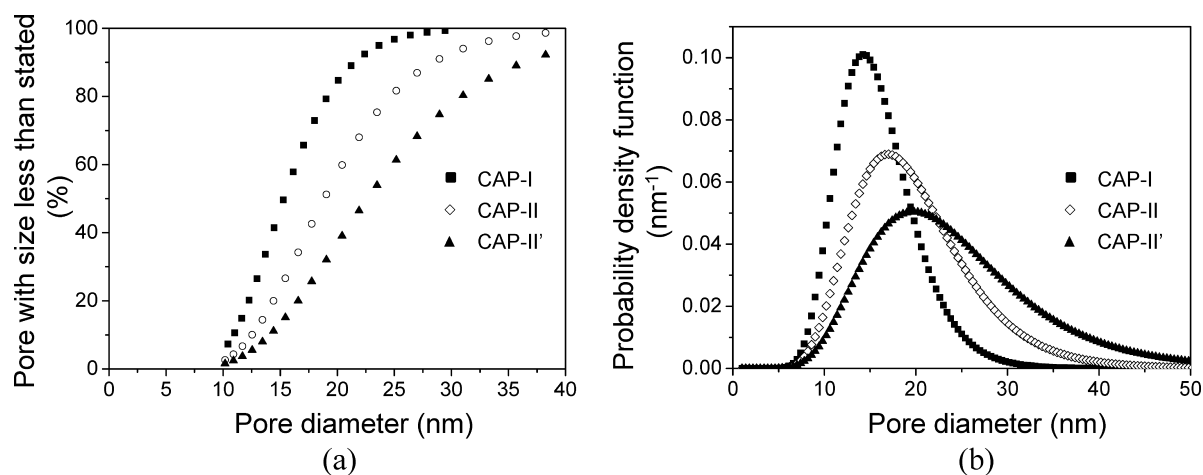


Figure 8. (a) Cumulative pore size distribution curves and (b) probability density function curves of the CAP substrates.

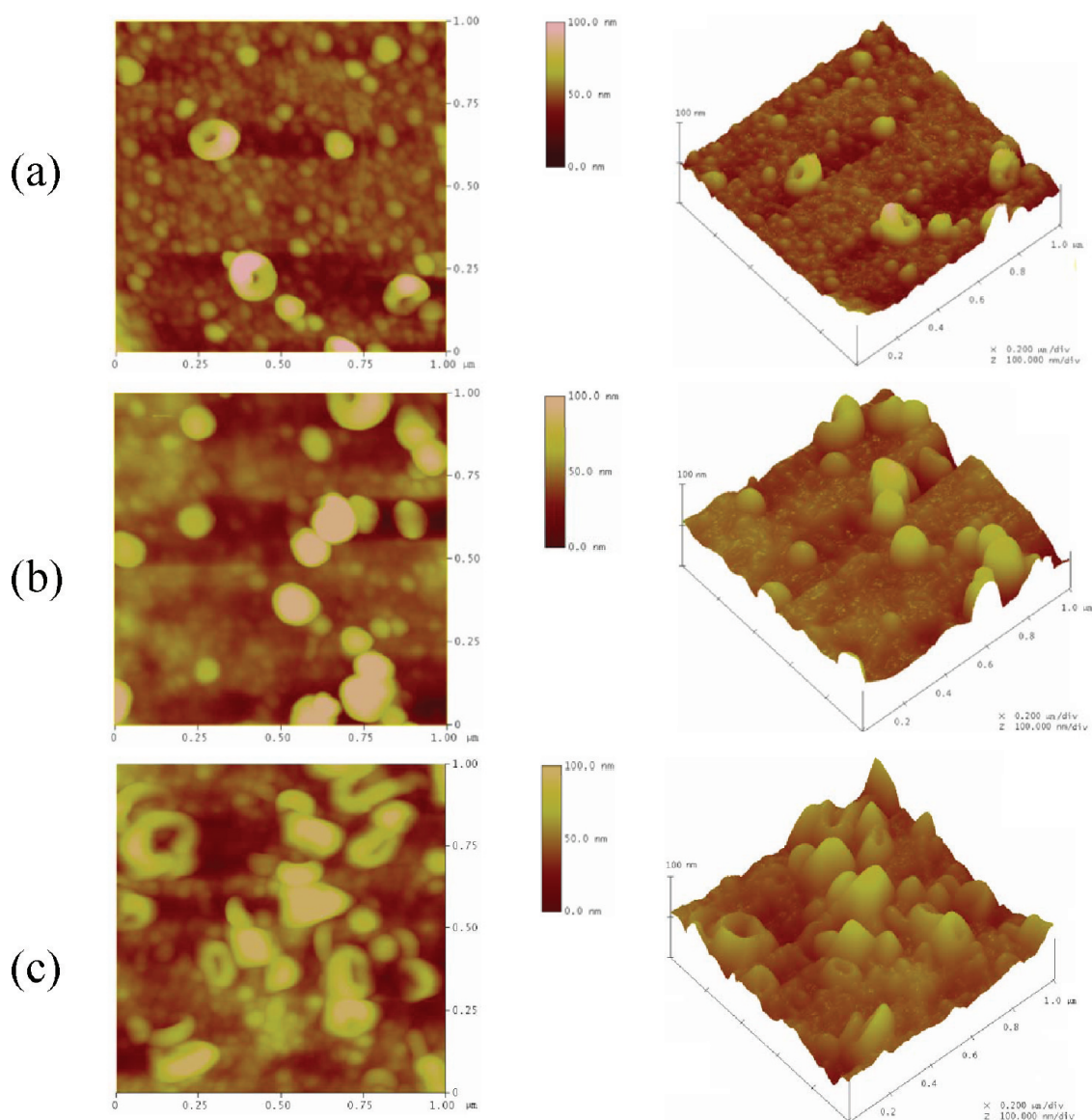


Figure 9. AFM image of the (a) CAP-I-TFC membrane, (b) CAP-II-TFC membrane, and (c) CAP-II'-TFC membrane.

understand their relationship, a third substrate was fabricated using the CAP-II polymer, designated as CAP-II'. Table 2 shows the dope formulation of the CAP-II' casting solution,

while Figure 7 illustrates the morphology of the substrate and TFC membrane. Table 6 compares the pore characteristics and MWCO properties of these three CAP substrates.

The cumulative pore size distribution curves and probability density function curves of these CAP substrates are depicted in Figure 8. It can be observed that the pore size distribution curve shifts toward the right (i.e., a larger size) and broader distribution from CAP-I to CAP-II, followed by CAP-II'.

Table 7. Surface Roughness of CAP-TFC FO Membranes

| membrane ID | R_a^a (nm) | R_{ms}^b (nm) |
|-------------|--------------|-----------------|
| CAP-I-TFC | 5.7 | 8.7 |
| CAP-II-TFC | 13.7 | 19.2 |
| CAP-II'-TFC | 16.6 | 21.8 |

^a R_a is the mean roughness. ^b R_{ms} is the root-mean-square of Z values.

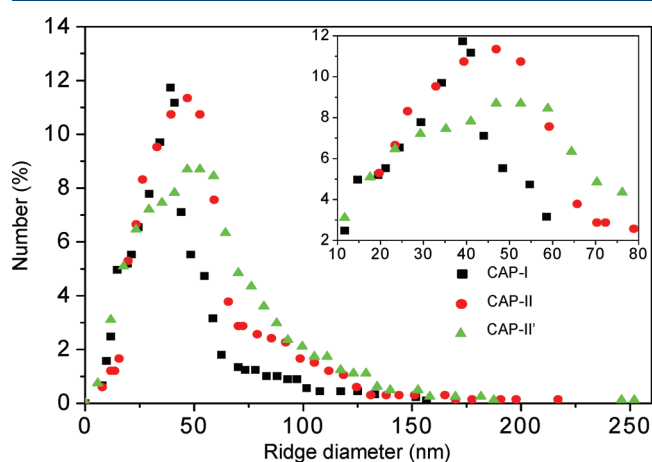


Figure 10. Size distribution curves of globular and worm-like structure on the CAP-TFC membranes.

The MWCO of CAP-I, CAP-II, and CAP-II' substrates are 136.0 kDa, 218.0 kDa, and 327.7 kDa, respectively. Among these three substrates, CAP-II' has the largest mean pore diameter of 22.7 nm as well as the broadest pore size distribution which may be beneficial to the formation of a rough ridge-valley or worm-like polyamide layer in the subsequently interfacial polymerization.

AFM tests were conducted to examine the surface topology of TFC membranes. Figure 9 illustrates the AFM images, while Table 7 summarizes the mean roughness and the root-mean-square of the Z value. A much rougher surface consisting of globular and worm-like morphology is observed in the CAP-II'-TFC membrane compared to the other two membranes. Figure 10 shows the size distribution of the globular and worm-like domains, obtained from an analysis of the AFM images. Interestingly, the domains' size distribution shifts to the right (i.e., toward large sizes) from the CAP-I-TFC membrane to the CAP-II'-TFC membrane, surprisingly similar to the aforementioned shift of the pore size distribution of the substrates. This consistency may provide a valuable insight to explain the effects of substrate pore morphology on the formation of the polyamide layer.

Figure 11 illustrates the dynamic evolution of interface formation. When a substrate is saturated by an aqueous PPD solution and is in contact with TMC organic solution, PPD molecules are erupting into the organic phase to react with TMC. Possessing small surface pores with narrower pore-size distributions, the CAP-I and CAP-II substrates are most likely to firmly hold the absorbed amine solution in the pores. Thus the interfacial reaction takes place at the meniscus near the organic side of the interface, while an amount of amine molecules must migrate from the narrow substrate pores to the organic phase.^{35,36,58} The inclusion of amine solution in

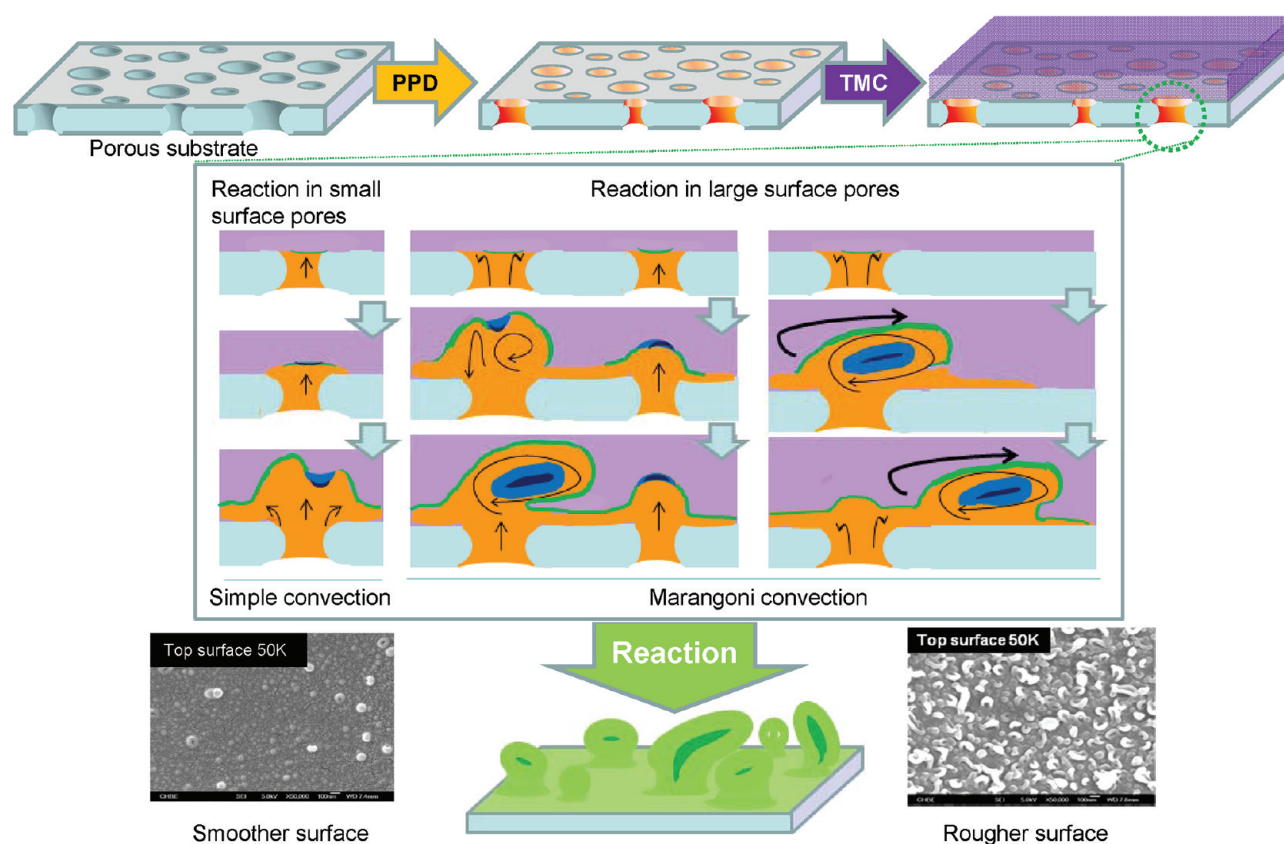


Figure 11. Conceptual model of TFC membrane formation.

smaller pores may result in the amine migration process mainly caused via diffusion and simple convection toward the interface. As a consequence, the interfacial reaction may initially produce nascent cross-linked films with small domain sizes, and the diffusion and simple convection processes do not in favor of forming a rougher globular and worm-like structure. The resultant TFC membrane has a smoother surface. In addition, since it takes time for PPD molecules to diffuse out of the small pores and react with TMC, the resultant polyamide layer may be less dense.

On the contrary, large pore sizes and a broader pore-size distribution of the CAP-II' substrate promote the rapid migration of amine molecules vigorously. Hence the Marangoni convection⁵⁹ may dominate over the simple convection at the interface, resulting in turbulent flow and enlarging the reaction contact area. On the other hand, large substrate pores enhance the PPD diffusion, leading to a fast interfacial reaction and rapid film growth with large domain sizes. Since the nascent ultrathin cross-linked large-domain films are floating on the substrate while fresh interfacial reactions are continuously evolving between unreacted TMC and PPD, the early cross-linked ultrathin domains may be pushed around, rotated, twisted, and bended by the turbulent flow and form the globular and worm-like structure when the interfacial polymerized film finally covers the entire substrate surface and impedes further reactants contact. Consequently, the reaction stops and a rough and compact selective polyamide layer forms. In summary, small surface pores of the substrate produce a smoother and less dense polyamide layer while large surface pores produce a rougher surface and more compact polyamide layer in the TFC membranes.

4. CONCLUSIONS

A series of TFC-FO membranes with enhanced FO performance have been prepared via an interfacial polymerization approach. Two kinds of hydrophilic CAP porous membranes with tailored structures were designed and used as substrates. The CAP-I substrate has a macrovoid-free sponge-like structure, while the CAP-II substrate possesses a finger-like structure spanning most of the cross-section. Even though these two substrates show completely distinct bulk morphology with each other, their TFC membranes show comparable membrane transport properties and FO performances. Both of them have low J_s/J_w ratio, high salt rejection, high pure water permeability, and high potential for seawater desalination. In addition, the effects of the pore morphology in the substrates on the formation of the polyamide layer were studied. An advanced scheme to form the globular and worm-like structure during the interfacial polymerization has been proposed. In general, small surface pores of the substrate facilitate simple convection at the interface during the interfacial reaction, produce nascent cross-linked films with small domain sizes, form a smoother and less dense structure, and reduce the possibility of defect formation. On the other hand, large surface pores promote the rapid migration of amine molecules, induce turbulent convection at the interface, and enlarge the reaction contact area, resulting in a rougher but more compact polyamide layer in the TFC membranes.

AUTHOR INFORMATION

Corresponding Author

*E-mail: chencts@nus.edu.sg. Tel.: (65) 6516-6645. Fax: (65) 6779-1936.

Notes

The authors declare no competing financial interest.

ACKNOWLEDGMENTS

The authors thank the Singapore National Research Foundation (NRF) for support through the Competitive Research Program for the project entitled, "New advanced FO membranes and membrane systems for wastewater treatment, water reuse, and seawater desalination" (Grant No. R-279-000-336-281) as well as Eastman Chemical Company for funding this research with through Grant No. R-279-000-315-597. Thanks are due to Miss. S. Zhang, Dr. N. Widjojo, Miss. H. Wang, Miss. P.S. Zhong, Miss. R.C. Ong, Dr. Y. Wang, and Miss. X.R. Teh for their useful comments and suggestions.

REFERENCES

- (1) Cornelissen, E. R.; Harmsen, D.; de Korte, K. F.; Ruiken, C. J.; Qin, J. J.; Oo, H.; Wessels, L. P. Membrane fouling and process performance of forward osmosis membranes on activated sludge. *J. Membr. Sci.* **2008**, 319, 158.
- (2) Kessler, J. O.; Moody, C. D. Drinking water from sea water by forward osmosis. *Desalination* **1976**, 18, 297.
- (3) McCutcheon, J. R.; McGinnis, R. L.; Elimelech, M. A novel ammonia-carbon dioxide forward (direct) osmosis desalination process. *Desalination* **2005**, 174, 1.
- (4) Chung, T. S.; Zhang, S.; Wang, K. Y.; Su, J. C.; Ling, M. M. Forward osmosis processes: yesterday, today and tomorrow. *Desalination* **2012**, 287, 78.
- (5) McCutcheon, J. R.; McGinnis, R. L.; Elimelech, M. Desalination by ammonia-carbon dioxide forward osmosis process: influence of draw and feed solution concentrations on process performance. *J. Membr. Sci.* **2006**, 278, 114.
- (6) Lee, K. L.; Baker, R. W.; Lonsdale, H. K. Membranes for power generation by pressure-retarded osmosis. *J. Membr. Sci.* **1981**, 8, 141.
- (7) Thorsen, T.; Holt, T. The potential for power production from salinity gradients by pressure retarded osmosis. *J. Membr. Sci.* **2009**, 335, 103.
- (8) Ling, M. M.; Chung, T. S. Novel dual-stage FO system for sustainable protein enrichment using nanoparticles as intermediate draw solutes. *J. Membr. Sci.* **2011**, 372, 201.
- (9) Dova, M. I.; Petrotos, K. B.; Lazarides, H. N. On the direct osmotic concentration of liquid foods. Part I. Impact of process parameters on process performance. *J. Food Eng.* **2007**, 78, 422.
- (10) Wang, K. Y.; Chung, T. S.; Qin, J. J. Polybenzimidazole (PBI) nanofiltration hollow fiber membranes applied in forward osmosis process. *J. Membr. Sci.* **2007**, 300, 6.
- (11) Yang, Q.; Wang, K. Y.; Chung, T. S. Dual-layer hollow fibers with enhanced flux as novel forward osmosis membranes for water production. *Environ. Sci. Technol.* **2009**, 43, 2800.
- (12) Su, J. C.; Yang, Q.; Teo, J. F.; Chung, T. S. Cellulose acetate nanofiltration hollow fiber membranes for forward osmosis processes. *J. Membr. Sci.* **2010**, 355, 36.
- (13) Wang, K. Y.; Ong, R. C.; Chung, T. S. Double-skinned forward osmosis membranes for reducing internal concentration polarization within the porous sublayer. *Ind. Eng. Chem. Res.* **2010**, 49, 4824.
- (14) Gerstandt, K.; Peinemann, K. V.; Skilhagen, S. E.; Thorsen, T.; Holt, T. Membrane processes in energy supply for an osmotic power plant. *Desalination* **2008**, 224, 64.
- (15) Wang, R.; Shi, L.; Tang, C. Y.; Chou, S.; Qiu, C.; Fane, A. G. Characterization of novel forward osmosis hollow fiber membranes. *J. Membr. Sci.* **2010**, 355, 158.
- (16) Yip, N. Y.; Tiraferri, A.; Phillip, W. A.; Schiffman, J. D.; Elimelech, M. High performance thin-film composite forward osmosis membrane. *Environ. Sci. Technol.* **2010**, 44, 3812.
- (17) Chou, S.; Shi, L.; Wang, R.; Tang, C. Y.; Qiu, C.; Fane, A. G. Characteristics and potential applications of a novel forward osmosis hollow fiber membrane. *Desalination* **2010**, 261, 365.
- (18) Tiraferri, A.; Yip, N. Y.; Phillip, W. A.; Schiffman, J. D.; Elimelech, M. Relating performance of thin-film composite forward

osmosis membranes to support layer formation and structure. *J. Membr. Sci.* **2011**, 367, 340.

(19) Wang, K. Y.; Chung, T. S.; Amy, G. Developing thin-film-composite forward osmosis membranes on the PES/SPSf substrate through interfacial polymerization. *AIChE J.* **2012**, 58, 770.

(20) Zhang, S.; Wang, K. Y.; Chung, T. S.; Chen, H.; Jean, Y. C.; Amy, G. Well-constructed cellulose acetate membranes for forward osmosis: Minimized internal concentration polarization with an ultra-thin selective layer. *J. Membr. Sci.* **2010**, 360, 522.

(21) Cadotte, J. E. Reverse osmosis membrane. US patent 4039440, 1977.

(22) Petersen, R. J. Composite reverse-osmosis and nanofiltration membranes. *J. Membr. Sci.* **1993**, 83, 81.

(23) Zou, L.; Vidalis, I.; Steele, D.; Michelmore, A.; Low, S. P.; Verberk, J. Q. J. C. Surface hydrophilic modification of RO membranes by plasma polymerization for low organic fouling. *J. Membr. Sci.* **2011**, 369, 420.

(24) Qin, J. J.; Wai, M. N.; Oo, M. H.; Wong, F. S. A feasibility study on the treatment and recycling of a wastewater from metal plating. *J. Membr. Sci.* **2002**, 208, 213.

(25) Yangali-Quintanilla, V.; Maeng, S. K.; Fujioka, T.; Kennedy, M.; Amy, G. Proposing nanofiltration as acceptable barrier for organic contaminants in water reuse. *J. Membr. Sci.* **2010**, 362, 334.

(26) Han, M. J.; Bhattacharyya, D. Thermal annealing effect on cellulose-acetate reverse-osmosis membrane-structure. *Desalination* **1995**, 101, 195.

(27) Su, J. C.; Chung, T. S. Sublayer structure and reflection coefficient and their effects on concentration polarization and membrane performance in FO processes. *J. Membr. Sci.* **2011**, 376, 214.

(28) Widjojo, N.; Chung, T. S.; Weber, M.; Maletzko, C.; Warzelhan, V. The role of sulphonated polymer and macrovoid-free structure in the support layer for thin-film composite (TFC) forward osmosis (FO) membranes. *J. Membr. Sci.* **2011**, 383, 214.

(29) Peng, W. H.; Escobar, I. C.; White, D. B. Effects of water chemistries and properties of membrane on the performance and fouling—A model development study. *J. Membr. Sci.* **2004**, 238, 33.

(30) Hong, S. K.; Escobar, I. C.; Hershey-Pyle, J.; Hobbs, C.; Cho, J. W. Biostability characterization in a full-scale hybrid NF/RO treatment system. *J. Am. Water Works Assoc.* **2005**, 97, 101.

(31) Zhao, S. F.; Zou, L. Effects of working temperature on separation performance, membrane scaling and cleaning in forward osmosis desalination. *Desalination* **2011**, 278, 157.

(32) Mi, B.; Elimelech, M. Chemical and physical aspects of organic fouling of forward osmosis membranes. *J. Membr. Sci.* **2008**, 320, 292.

(33) Mi, B.; Elimelech, M. Organic fouling of forward osmosis membranes: Fouling reversibility and cleaning without chemical reagents. *J. Membr. Sci.* **2010**, 348, 337.

(34) Xu, T.; Farris, R. J. Comparative studies of ultra-high molecular weight polyethylene fiber reinforced composites. *Polym. Eng. Sci.* **2007**, 47, 1544.

(35) Singh, P. S.; Joshi, S. V.; Trivedi, J. J.; Devmurari, C. V.; Prakash Rao, A.; Ghosh, P. K. Probing the structural variations of thin film composite RO membranes obtained by coating polyamide over polysulfone membranes of different pore dimensions. *J. Membr. Sci.* **2006**, 278, 19.

(36) Ghosh, A. K.; Hoek, E. M. V. Impacts of support membrane structure and chemistry on polyamide-polysulfone interfacial composite membranes. *J. Membr. Sci.* **2009**, 336, 140.

(37) Cadotte, J. E.; Rozelle, L. T.; Petersen, R. J.; Francis, P. S. Water transport across ultrathin membranes of mixed cellulose ester and ether derivatives. *Appl. Polym. Symp.* **1970**, 13, 73.

(38) Kutowy, O.; Matsuura, T.; Sourirajan, S. Permeation characteristics of cellulose acetate propionate reverse osmosis membranes. *Can. J. Chem. Eng.* **1976**, 54, 364.

(39) Shintani, T.; Matsuyama, H.; Kurata, N. Effect of heat treatment on performance of chlorine-resistant polyamide reverse osmosis membranes. *Desalination* **2009**, 247, 370.

(40) Wang, K. Y.; Matsuura, T.; Chung, T. S.; Guo, W. F. The effects of flow angle and shear rate within the spinneret on the separation performance of poly(ethersulfone) (PES) ultrafiltration hollow fiber membranes. *J. Membr. Sci.* **2004**, 240, 67.

(41) Sun, S. P.; Wang, K. Y.; Peng, N.; Hatton, T. A.; Chung, T. S. Novel polyamide-imide/cellulose acetate dual-layer hollow fiber membranes for nanofiltration. *J. Membr. Sci.* **2010**, 363, 232.

(42) Bowen, W. R.; Mohammad, A. W. Characterization and prediction of nanofiltration membrane performance—A general assessment. *Chem. Eng. Res. Des.* **1998**, 76, 885.

(43) Youm, K. H.; Kim, W. S. Prediction of intrinsic pore properties of ultrafiltration membrane by solute rejection curves: Effects of operating conditions on pore properties. *J. Chem. Eng. Jpn.* **1991**, 24, 1.

(44) Wang, K. Y.; Chung, T. S. The characterization of flat composite nanofiltration membranes and their applications in the separation of Cephalexin. *J. Membr. Sci.* **2005**, 247, 37.

(45) Zhang, S.; Wang, K. Y.; Chung, T. S.; Jean, Y. C.; Chen, H. Molecular design of the cellulose ester-based forward osmosis membranes for desalination. *Chem. Eng. Sci.* **2011**, 66, 2008.

(46) Loeb, S.; Mehta, G. D. A two-coefficient water transport equation for pressure-retarded osmosis. *J. Membr. Sci.* **1979**, 4, 351.

(47) Lobo, V. M. M. Mutual diffusion coefficients in aqueous electrolyte solutions (technical report). *Pure Appl. Chem.* **1993**, 65, 2613.

(48) Chen, H.; Hung, W. S.; Lo, C. H.; Huang, S. H.; Cheng, M. L.; Liu, G.; Lee, K. R.; Lai, J. Y.; Sun, Y. M.; Hu, C. C.; Suzuki, R.; Ohdaira, T.; Oshima, N.; Jean, Y. C. Free-volume depth profile of polymeric membranes studied by positron annihilation spectroscopy: Layer structure from interfacial polymerization. *Macromolecules* **2007**, 40, 7542.

(49) Tung, K. L.; Jean, Y. C.; Nanda, D.; Lee, K. R.; Hung, W. S.; Lo, C. H.; Lai, J. Y. Characterization of multilayer nanofiltration membranes using positron annihilation spectroscopy. *J. Membr. Sci.* **2009**, 343, 147.

(50) Shintani, T.; Shimazu, A.; Yahagi, S.; Matsuyama, H. Characterization of methyl-substituted polyamides used for reverse osmosis membranes by positron annihilation lifetime spectroscopy and MD simulation. *J. Appl. Polym. Sci.* **2009**, 113, 1757.

(51) Coleman, P. *Positron Beams and Their Applications*; World Scientific Publishing: Singapore, 2000.

(52) Jean, Y. C.; Mallon, P. E.; Schrader, D. M. *Principles and Applications of Positron and Positronium Chemistry*; World Scientific Publishing: Singapore, 2003.

(53) Li, F. Y.; Li, Y.; Chung, T. S.; Chen, H.; Jean, Y. C.; Kawi, S. Development and positron annihilation spectroscopy (PAS) characterization of polyamide imide (PAI)-polyethersulfone (PES) based defect-free dual-layer hollow fiber membranes with an ultrathin dense-selective layer for gas separation. *J. Membr. Sci.* **2011**, 378, 541.

(54) Chen, H. Z.; Xiao, Y. C.; Chung, T. S. Multi-layer composite hollow fiber membranes derived from poly(ethylene glycol) (PEG) containing hybrid materials for CO₂/N₂ separation. *J. Membr. Sci.* **2011**, 381, 211.

(55) Wei, J.; Qiu, C.; Tang, C. Y.; Wang, R.; Fane, A. G. Synthesis and characterization of flat-sheet thin film composite forward osmosis membranes. *J. Membr. Sci.* **2011**, 372, 292.

(56) Phillip, W. A.; Yong, J. S.; Elimelech, M. Reverse draw solute permeation in forward osmosis: Modeling and experiments. *Environ. Sci. Technol.* **2010**, 44, 5170.

(57) Gray, G. T.; McCutcheon, J. R.; Elimelech, M. Internal concentration polarization in forward osmosis: Role of membrane orientation. *Desalination* **2006**, 197, 1.

(58) Freger, V. Kinetics of film formation by interfacial polycondensation. *Langmuir* **2005**, 21, 1884.

(59) Zeytounian, R. K. *Convection in Fluids*; Springer: Dordrecht, 2009.